POLITECNICO DI TORINO
Repository ISTITUZIONALE

Effect of inert gas pressure on the properties and carbon footprint of UNS S32760 powders made from waste materials by gas atomization

(Article begins on next page)

22 December 2024

Effect of inert gas pressure on the properties and carbon footprint of UNS S32760 powders made from waste materials by gas atomization

Federico Simone Gobber [a,c,d,*], Paolo C. Priarone [b,d], Antonio Pennacchio [a,c], Marco Actis Grande [a,c,d]

[a] Politecnico di Torino, Department of Applied Science and Technology, Viale Teresa Michel 5, 15121, Alessandria, Italy
[b] Politecnico di Torino, Department of Management and Production Engineering, Corso Duca degli Abruzzi 24, 10129, Torino, Italy
[c] Consorzio INSTM, Via Giusti 9, 50121, Firenze, Italy
[d] Interdepartmental Center IAM@PoliTo - Integrated Additive Manufacturing, Corso Duca degli Abruzzi 24, 10129, Torino, Italy

ARTICLE INFO

ABSTRACT

Super duplex steels are used in various industrial applications where high mechanical strength and corrosion resistance are required. The manufacture of products from powdered base materials has become increasingly interesting in recent years, both for traditional powder metallurgy processes and for additive manufacturing. Due to the high environmental impact of the raw material, which is higher than that of austenitic or martensitic stainless steels, sustainable powder production routes are therefore needed. This research focuses on the production, characterization and sustainability assessment of UNS S32760 super duplex steel powders produced by gas atomization from industrial waste materials. The critical role of gas atomization pressure in determining the process efficiency, properties and carbon footprint of the powders is analyzed. The results show that higher gas pressure leads to narrower atomization plumes and higher gas velocities, with a significant increase in gas consumption and longer atomization cycles. Morphological analysis showed that increasing gas pressure improved atomization efficiency. However, it also resulted in increased powder surface roughness and pore formation. Chemical composition was minimally affected by gas pressure. Energy demand and carbon footprint analyses showed that higher gas pressure reduced the carbon footprint as powder size decreased. Overall, the study shows that adjusting the atomization pressure can reduce the carbon footprint based on the desired final powder size distribution, and provides useful information for improving powder production processes to promote sustainable manufacturing practices.

1. Introduction

Duplex stainless steels are known for their high mechanical strength and corrosion resistance [1]. They find extensive applications in the oil and gas [2] and chemical [3] industries, and have recently been considered for use in biomedical prosthetic devices [4]. These steels contain both ferrite stabilizers (e.g., chromium, silicon, molybdenum) and austenite stabilizers (e.g., carbon, nickel, nitrogen), resulting in a duplex microstructure with nearly equal amounts of ferrite and austenite. This microstructure improves corrosion resistance in chlorinated environments, particularly with regard to stress corrosion cracking and pitting corrosion, while providing greater strength than standard austenitic stainless steels such as AISI 304 or AISI 316. In addition, duplex stainless steels exhibit remarkable resistance to atmospheric corrosion, eliminating the need for painting or significant maintenance in aggressive atmospheres [5]. Moreover, their high strength allows for thickness savings, making them a cost-effective alternative to painted carbon steel over their life cycle [6].

Traditional powder metallurgy processing of super duplex stainless steels (SDSS) has been explored in recent decades with respect to pressing and sintering [7] and hot isostatic pressing [8]. More recently, the interest has focused on the additive manufacturing of duplex stainless steels [9]. Within the super duplex grades, most of the literature has focused on the processability properties of the additively manufactured UNS S32750 grade (also referred to as EN 1.4410, AISI F53, X2CrNiMoN25-7-4) by L-PBF [10], directed energy deposition [11], wire arc additive manufacturing [12], electron beam melting [13], while the UNS S32760 grade (EN 1.4501, AISI F55,

---

X2CrNiMoCuWN25-7-4) has received less attention. The lack of studies on this topic is likely due to the limited availability of commercial powders.

To understand the critical role of powder properties in its process-ability, factors such as particle size distribution (PSD), particle shape, powder flowability and apparent density must be considered and optimized to produce high-quality powder layers during spreading [14]. Spherical powders generally exhibit superior flowability and spreadability, yielding powder layers with high density and as-built parts with low porosity. Conversely, irregularly-shaped particles impede flowability due to interlocking mechanisms, while very fine particles lead to agglomeration and reduced flowability. Metal powders for laser additive manufacturing are typically produced by gas atomization. The gas atomization process and its parameters, including atomization gas pressure, melt delivery tube diameter, and melting temperature [15] significantly affect powder properties. Additionally, atomization gas temperature and type affect particle size, shape, chemistry, and quality. Hot gas increases sonic velocity, resulting in smaller, spherical droplets, as observed by Cui et al. [16]. The choice of process gas, whether nitrogen or argon, contributes to variations in the composition of the steel melt and can even result in the encapsulation of argon, creating hollow particles. The interaction of these process parameters and conditions has a significant impact on the powder properties and, consequently, on the quality of powder metallurgical (P/M) parts. To the best of the authors' knowledge, the work of Cui et al. [16] is currently the only contribution in the literature on the production of UNS S32760 powders tailored for the L-PBF process. They investigated the effect of the gas used (argon or nitrogen) and its temperature (room temperature or heated to 330 °C) on the quality of the produced powders.

The exploration of the influence of the atomizing gas inlet pressure, its correlation with powder properties and its impact on the sustainability of the gas atomization process in relation to the final application of the powder use is currently a work in progress for the authors [17–19]. The research presented in this paper focuses on the production, characterization and sustainability assessment of UNS S32760 super duplex steel powders produced by gas atomization from industrial waste materials. First, the effect of varying the atomization gas pressure in the range of 30–45 bar on gas consumption and process yield is evaluated. Then, the properties of the atomized powders are analyzed to validate their quality. Finally, the sustainability concerns are discussed in terms of the carbon footprint of the powders produced.

2. Materials and methods

Stud bolts and nuts made of UNS S32760 SDSS, which had been discarded by the manufacturer after being evaluated for geometric non-compliance with customer standards, were collected. The chemical composition of the incoming wrought material (given in Table 1) was determined using a Metal Lab Plus optical emission spectroscope by GNR and a Leco CS 744 carbon/sulfur analyzer. The parts were cleaned in an ultrasonic cleaning bath using a Logimec Srl model 5 RS cleaner. Batches of a mixture of nuts and bolts weighing 5.2 ± 0.3 kg were loaded into an alumina crucible (as shown in Fig. 1*a*) and melted under a shielding, non-reactive argon atmosphere (Fig. 1*b*); the powders were

then produced by inert gas atomization with argon (Fig. 1*c*). The atomization setup is presented in Section 2.1. The as-atomized powders were then sieved and characterized as described in Section 2.2, and their energy demand and carbon footprint were quantified as detailed in Section 2.3.

2.1. Atomization setup

The powder atomization was carried out using a Vacuum Inert Gas Atomizer (VIGA) in a close-coupled configuration, schematically represented in Fig. 2, equipped with an Ambrell EKOHEAT 20/25 induction unit and a Hitema ENR 022 cooling unit. The main process parameters are listed in Table 2. After evacuating the atomizer to $6 \cdot 10^{-3}$ mbar, the material was inductively heated at a heating rate of 18 ± 4 °C/min to avoid thermal shocks to the alumina crucible. As the heating progressed, the induction parameters were gradually increased (i.e., power from 3 to 12 kW, frequency from 6 to 7 kHz, and voltage from 110 to 200 V) to maintain a stable heating rate. When the temperature reached approximately 1000 °C, both the melting and atomization chambers were backfilled with argon to prevent volatile elements from leaving the molten bath. The atomization chamber was then set at atmospheric pressure, while the melting chamber was set at a slight overpressure (0.05 barg) with a fluxing atmosphere. A homogeneous molten bath was obtained at 1440 ± 10 °C, and an additional 200 °C overheating was set [17].
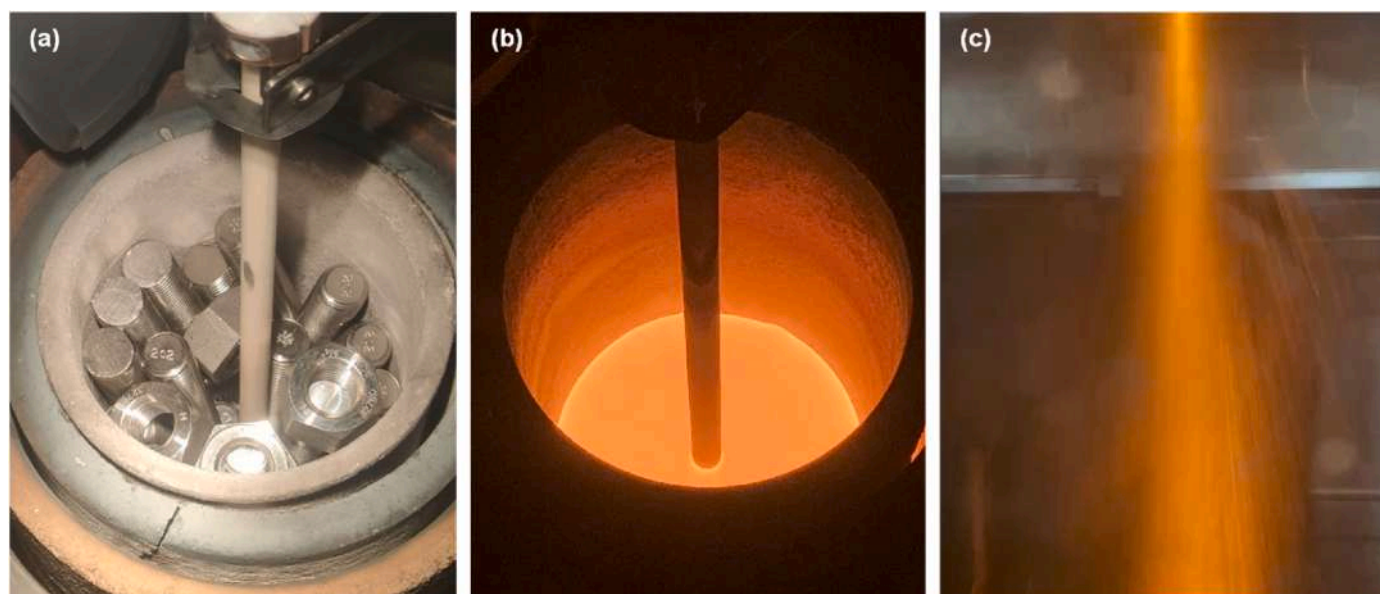
A pressure of 0.25 barg was then applied to the melting chamber in order to force the flow of molten metal into the atomization chamber through a 2.4 mm-diameter melt delivery nozzle. This nozzle was attached to an 88 mm-long melt delivery tube. The pressure in the atomization chamber was kept constant throughout all the experiments, while a pressure of 0.04–0.05 barg was recorded in the atomization tower during all the atomization runs. Four different atomization pressures (*p*) were considered, each increasing the inlet pressure by 5 bar from 30 to 45 bar. The lower limit of 30 bar and the upper limit of 45 bar were chosen based on previous experience: the atomization pressure below 30 bar results in a high proportion of coarse powders not useable for AM processes, while increasing the pressure above 45 bar affects the stability of the gas atomization with a higher risk of metal freezing at the melt delivery tube. Each atomization lasted approximately 3–5 min before the heating was turned off and the atomized powders were allowed to cool. Most of the atomized powders were collected in the primary hopper, while a small fraction was separated from the exhaust argon by a cyclone and collected in a secondary hopper (Fig. 2). The atomization yield was determined by dividing the mass of powder collected from the primary and secondary hoppers by the amount of material loaded into the crucible. Powders from each atomization test were mixed in separate batches to homogenize the distribution and avoid segregation, sieved through a 250 μm sieve to remove atomization debris, and then characterized.

2.2. Powder characterization

Two different characterization routes were followed, with some analyses performed on the entire PSD (Section 2.2.1) and others isolating more specific portions (Section 2.2.2).

2.2.1. PSD, morphology and true density

The powder size distribution (PSD) for each atomization condition was measured on dried samples by laser granulometry (using a Mastersizer 3000) with 15% feed and 3.0 bar of carrier gas, assuming spherical powders and the coefficient of reflectivity proper of stainless steels, as taken from the Malvern database. The PSD was measured on the full range of powders atomized in each run, after sieving the large atomized debris over 250 μm in size. For powder morphology, qualitative and quantitative observations were made either by scanning electron microscopy (using a Zeiss EVO 15 SEM equipped with

Table 1
Wrought material composition in weight percent.

Element	wt. %	Element	wt. %
Carbon, C	0.015 ± 0.001	Cobalt, Co	0.065 ± 0.001
Chromium, Cr	25.80 ± 0.03	Niobium, Nb	0.02 ± 0.004
Nickel, Ni	7.15 ± 0.04	Vanadium, V	0.05 ± 0.001
Silicon, Si	0.406 ± 0.002	Nitrogen, N	0.20 ± 0.003
Manganese, Mn	0.627 ± 0.003	Titanium, Ti	<0.001
Molybdenum, Mo	3.60 ± 0.01	Phosphorus, P	<0.02
Copper, Cu	0.65 ± 0.01	Sulfur, S	<0.004
Tungsten, W	0.62 ± 0.004	Iron, Fe	Balance

Fig. 1. Schematic of the powder production route: (*a*) crucible loading with non-compliant stud bolts and nuts, (*b*) melting and temperature homogenization, (*c*) powder production by inert-gas atomization.

backscattered and secondary electron probe) or by quantitative automated optical image analysis (using a Malvern Morphologi 4). The true density of the powders was measured using an Anton Paar Ultrapyc 3000 helium pycnometer, and to better understand the process-related characteristics, two different PSDs were also measured, taking into account the powder applications: (*i*) 20–63 μm used for L-PBF, and (*ii*) 63–150 μm used for EBM or DED.

2.2.2. Light elements and structural characterization

In order to obtain information on the light element content while taking into account the specific surface area of different powder sizes, the overall PSD was further subdivided into three narrower intervals: <20 μm, 53–63 μm, and 106–120 μm. Carbon (C) and sulfur (S) contents were determined by non-dispersive infrared (NDIR) measurement after powder combustion (using a Leco CS 744 analyzer), while oxygen (O), nitrogen (N), and hydrogen (H) contents were determined by NDIR measurement after melting under inert gas with helium as the carrier medium (using a Leco ONH 836 analyzer). The method used for the measurement of carbon, sulfur, oxygen and nitrogen is based on the ASTM E1019 standard. In contrast, the measurement of hydrogen is not standardized, although it is widely used in both steelmaking and scientific research studies. Three replicates were carried out for each test, with samples weighing approximately 1.00 ± 0.01 g. The powder composition in terms of elements heavier than C was determined by EDS (using an Oxford Ultim max) on the cross section of samples mounted in resin and metallographically prepared with diamond suspensions (6, 3 and 1 μm) and colloidal silica. The amounts of austenite/ferrite in both the powders and wrought material were measured by X-ray diffraction (XRD). A Pulstec μ-X360s diffractometer intended for measuring residual stresses and retained austenite was employed; the instrument has a Cr anode operating at 30 kV - 1.5 mA and is equipped with a 2D detector. The analysis was reduced to the 120–175° 2θ interval, where both austenite and ferrite peaks are present. Another set of XRD analyses was performed on a Malvern Empyrean diffractometer for phase analysis to determine the crystallite size for the three PSD narrow intervals at the extreme values of the selected atomization pressure range (i.e., 30 and 45 bar).

2.3. Energy and carbon footprint assessment

Primary energy demand and equivalent carbon dioxide (CO_2) emissions were analyzed by applying and extending the methodology presented by the authors in Ref. [17]. Both metrics were quantified for each test while varying the atomization gas pressure. The carbon footprint was then calculated for the unit mass of powders with dimensions (*i*) < 20 μm, to be used for MIM and BJ; (*ii*) 20–63 μm, to be used for L-PBF; and (*iii*) 63–150 μm, to be used for EBM and DED. The atomization process after the recovery of the UNS S32760 industrial waste is considered in the system boundary labeled 'A' in Fig. 3. Impacts were calculated based on the energy and resource consumption associated with (*i*) preliminary waste preparation, (*ii*) gas atomization and (*iii*) powder sieving. In this case, the waste preparation phase was limited to the cleaning step, as no cutting operations were required because the size of the recovered parts was already compatible with the crucible size, allowing complete filling without the need for further fractionation of the recovered parts (Fig. 1a). In addition, to verify the potential reduction in environmental impact associated with the production of metal powders directly from waste streams, the results of the carbon footprint assessment were benchmarked with those obtained by applying the same gas atomization route to incoming feedstock from primary and/or secondary material production, according to Ref. [20], and the system boundary labeled 'B' in Fig. 3 was considered.

3. Results and discussion

The main results related to the variation of the atomization gas pressure are presented and discussed in the following in terms of (*i*) process performance (Section 3.1), (*ii*) characterization (Section 3.2), and (*iii*) primary energy demand and carbon footprint of the produced powders (Section 3.3).

3.1. Process characterization results

Increasing the atomization gas pressure (*p*) increases the gas velocity at the outlet of the convergent-divergent annular nozzle and tightens the atomization plume, as shown in Fig. 4. According to the results of CFD studies reported in Ref. [21] for a comparable atomization unit, the gas velocity is supersonic (the sound velocity for argon at 1 bar is ≈ 320
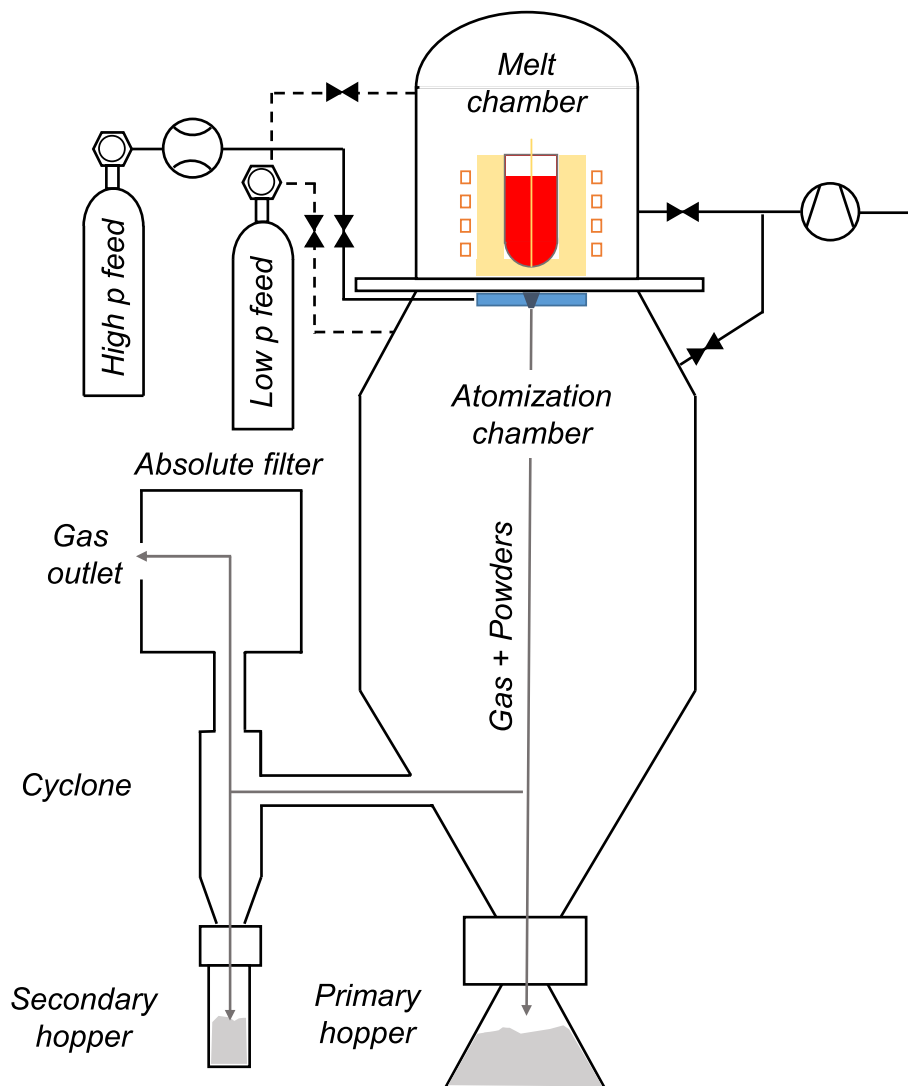
Fig. 2. Schematic diagram of the CC-VIGA unit.

Table 2
Main process parameters for the atomization of UNS S32760 SDSS.

Parameter	Value
Loaded material	5.2 ± 0.3 kg
Liquidus temperature	1440 ± 10 °C
Overheating	200 °C
Melting chamber pressure	0.25 barg
Atomization gas pressure, p	30; 35; 40; 45 bar
Average atomization gas mass flow	2.29; 2.78; 2.79; 3.07 kg/min
Average metal mass flow	1.73; 1.08; 0.84; 0.88 kg/min
Gas-to-metal ratio, GMR	1.32; 2.57; 3.32; 3.49

m/s) when disrupting the molten metal fillet at the outlet of the melt delivery tube. A pressure higher than 2 bar is developed at the bottom of the atomization nozzle, corresponding to the first supersonic shock wave generated by the high-speed gas [21]. In the present work, increasing the gas velocity resulted in longer atomization cycles (from less than 3 min at 30 bar to more than 5 min at 45 bar). An increase in the pressure at the melt delivery nozzle is supposed to occur, as observed in Ref. [22]. Such a mechanism can explain the relevant increase in argon consumption during the atomization process despite the slight increase in the gas flow rate, as shown in Table 3.

As the gas velocity increases, its temperature decreases due to the higher expansion. In fact, after expanding through the convergent-divergent annular nozzle, the gas is at 1.04 bar, as measured by pressure sensors installed in the atomization chamber. The argon expansion in the gas atomization nozzle is adiabatic, not isothermal, so the gas temperature drops significantly after the expansion. Temperatures as low as −5 °C to −25 °C have been measured using K-thermocouples for the sole expanding gas at inlet pressures from 30 to 45 bar. Gas cooling can have two distinct effects on the process: (*i*) the total gas consumption tends to increase as the gas temperature progressively decreases, and (*ii*) the molten metal can freeze at the melt delivery nozzle with the risk of blocking the atomization or, in the most favorable case, causing frequent instabilities in the atomization plume stream [23]. In the tests performed in this study, continuous and stable atomization plumes were observed for atomization gas pressures from 30 to 40 bar, while increasing the pressure to 45 bar resulted in a periodically unstable atomization plume characterized by frequent melt interruptions. However, the effects of such interruptions are not directly observable in the fraction of atomization debris produced. Although a general decreasing trend is observed as the gas pressure increases from 30 to 40 bar, the slight increase in the amount of atomization debris when the pressure is increased to 45 bar is not considered significant. This variation is only a few grams, which is within the range of experimental reproducibility of the atomization runs (Fig. 5a). In addition, the powders are carried to the primary hopper by the high velocity stream of inert argon. As the
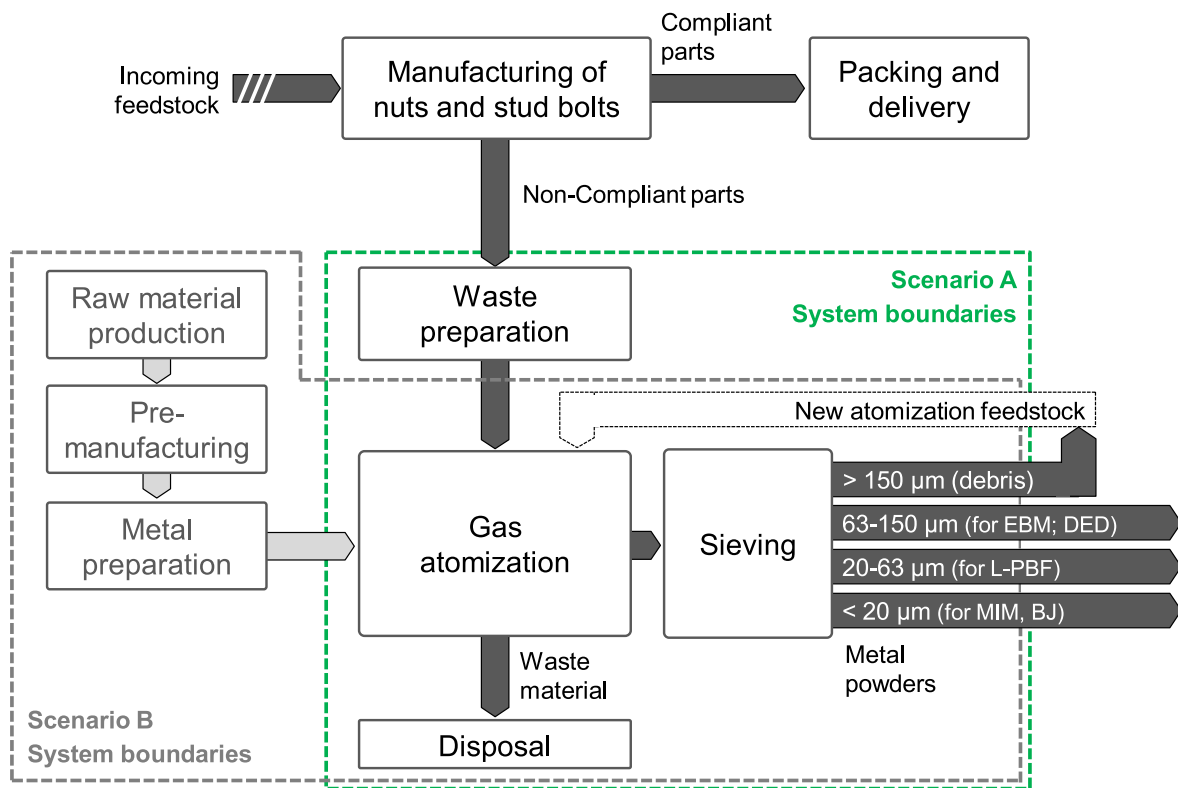
Fig. 3. System boundaries for the environmental impact assessment (extended from Ref. [17]).
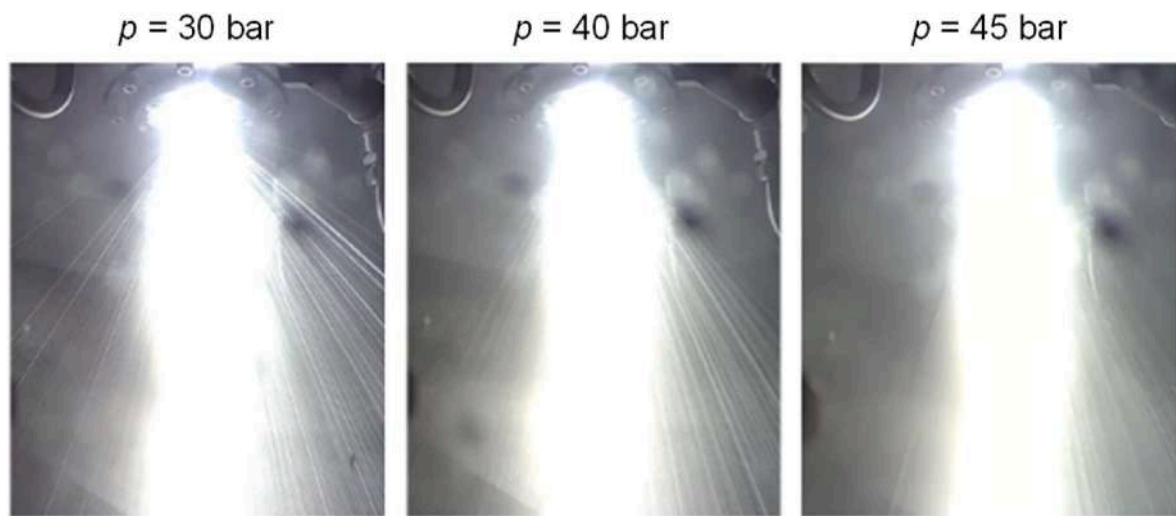

Fig. 4. Experimental observation of the atomization plume as the gas pressure (*p*) is varied.

Table 3
Argon consumption (including atomization and backfilling) [17].

Atomization gas pressure, *p*	Argon consumption		
	Atomization	Backfilling	Total
30 bar	6.5 kg	1.0 kg	7.5 kg
35 bar	13.9 kg	0.8 kg	14.7 kg
40 bar	15.5 kg	0.9 kg	16.4 kg
45 bar	17.0 kg	1.1 kg	18.1 kg

atomization mechanisms become more efficient, a higher fraction of fine powders is produced and collected in the secondary hopper after being separated by a cyclone positioned before the absolute filter, and the fraction of powders collected in the primary hopper is consequently reduced when the atomization gas pressure is increased (Fig. 5*b*).

3.2. Powder characterization results

This section presents the results of powder characterization, performed according to the procedures described in Section 2.2, in terms of (*i*) powder size distribution (Section 3.2.1), (*ii*) true density (Section 3.2.2), (*iii*) qualitative morphology (Section 3.2.3), (*iv*) chemical composition (Section 3.2.4), and (*v*) quantitative morphological
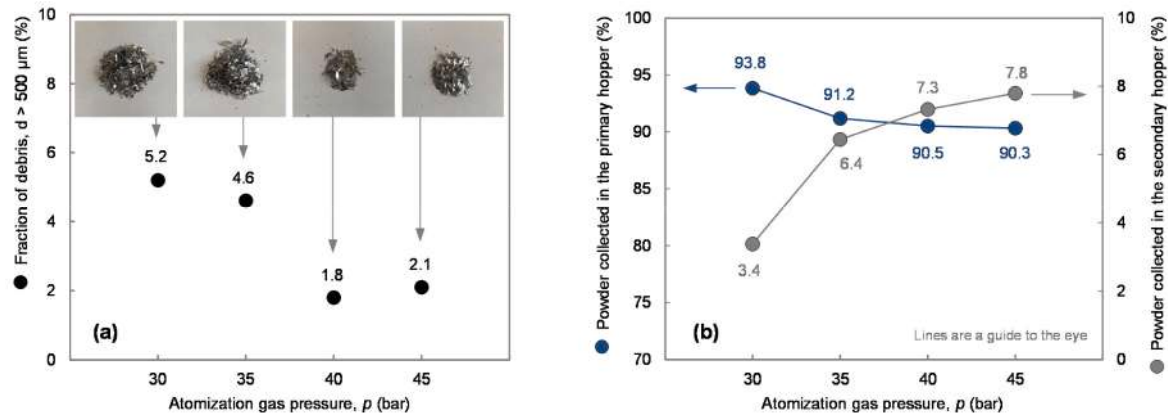
Fig. 5. Amount of atomization debris collected in the primary hopper (*a*) and overall amount of material collected in the primary and secondary hopper (*b*).

properties (Section 3.2.5).

3.2.1. Powder size distribution (PSD)

The overall powder size distribution (PSD) shifts to lower values as the atomization gas pressure increases (Fig. 6*a* and *b*), as expected. This decreasing trend is particularly evident from 30 to 40 bar, with the average powder size indicator D_{50} decreasing linearly. A further increase in atomization gas pressure (that is, in gas velocity) to 45 bar does not appear to be effective in reducing the PSD. The tests performed at 40 and 45 bar give very close results, with a slight increase in the granulometric indicators D_{50} and D_{90}, as shown in Table 4. Two different effects are supposed to be the cause of this deviation from the expected trend. Although it is well known that an increase in the atomization gas pressure should lead to a decrease in PSD, it is also evident that instabilities of the atomization plume lead to deviations from this expected behavior. Furthermore, as reported in the literature [24], the particle sizes cannot be significantly reduced with each further increase in atomization pressure due to capacity limitations of the gas atomization system. If the atomization plume is unstable, the primary and secondary atomization mechanisms are altered by the pulsating regime [25]; a steady continuous flow is not achieved during the process, resulting in larger-than-expected particles. Second, if the increase in gas pressure does not significantly affect the atomization mechanisms, more intense internal recirculating flows will be generated by the higher amount of gas at a higher velocity. It is known that gas flow recirculation becomes

Table 4
Granulometric metrics (D_{10}, D_{50} and D_{90}) as a function of atomization gas pressure [17].

Atomization gas pressure, *p*	D_{10} (µm)	D_{50} (µm)	D_{90} (µm)
30 bar	34.2	91.6	248.1
35 bar	27.3	75.9	230.8
40 bar	21.7	61.2	155.6
45 bar	21.6	64.1	195.6

particularly critical in the upper part of the atomization chamber and is responsible for the incorporation of small powder particles on the surface of larger powders, forming the so-called satellites. As the gas velocity increases and the gas flow in the chamber increases, the recirculation zones at the top of the gas atomizer can become more severe [26]. Increasing the gas atomization pressure from 40 to 45 bar results in further gas consumption without significantly reducing the final powder size. Based on the process characterization of yield in specific granulometric intervals suitable for AM processes, the most effective atomization pressure to reduce the PSD appears to be 40 bar. It should be noted that these atomization pressure values are valid for the configuration adopted in this study; differences in the inlet absolute value are expected if the atomizer geometry is changed or if the gas flow rate or the melt flow rate are modified by changing the melt delivery nozzles or the gas nozzle designs.
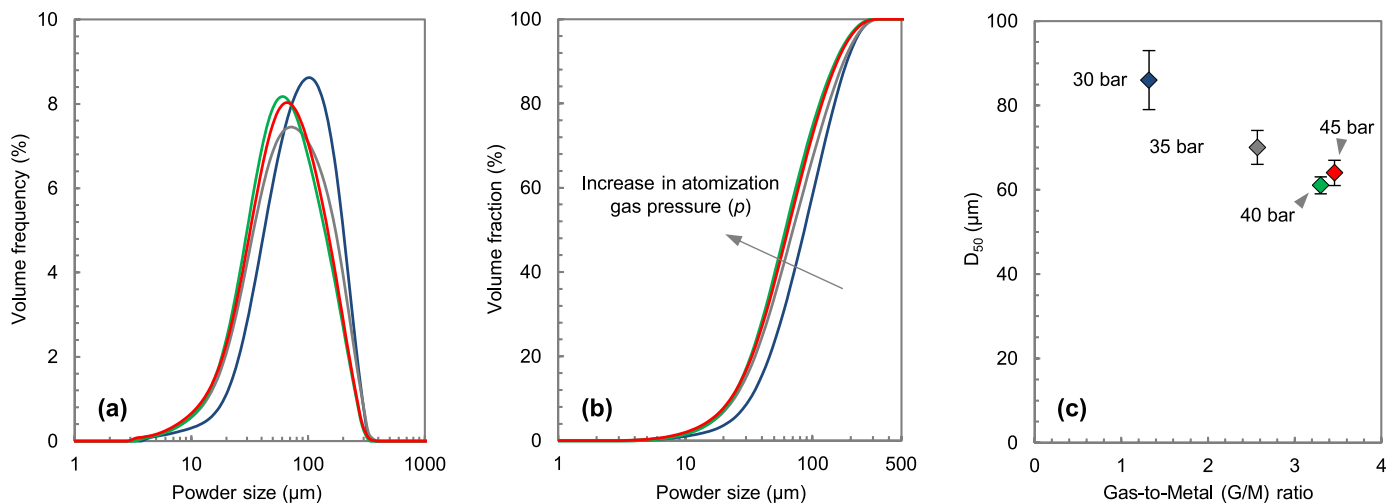

Fig. 6. Volume particle size distribution (*a*), cumulative particle size distribution (*b*) and correlation between D_{50} and G/M ratio (*c*).

The Gas-to-Metal ratio (G/M), either in mass [27] or volume [28], is a fundamental indicator of the efficiency of gas atomization process. When correlated with the Particle Size Distribution (PSD), as in Fig. 6c, it allows the efficiency of different gas atomizers to be compared. Generally, the total amount of gas consumed during atomization is considered to estimate the G/M, but theoretically, this G/M is not constant throughout the process. On the one hand, the liquid metal flow during atomization is not constant, as the metallostatic force decreases as the crucible is gradually emptied. On the other hand, the atomization pressure is usually kept constant from start to finish. An additional pressure to the metallostatic one is generally applied in the melt chamber to force the molten metal to flow through the melt delivery tube, where capillary forces tend to hinder the molten metal from flowing [29].

3.2.2. True density

The true density of powders was measured to determine the interaction between argon and the powder formation. As reported in the literature [16], a true density lower than that of the bulk material is expected for powders as their size increases due to the formation of internal porosity. In Fig. 7, a linear decreasing trend in true density with increasing the atomization gas pressure can be observed for powders in the 63–150 μm range, while the values are more scattered for powders in the 20–63 μm range. A hypothetical reduction in true density could be related to a change in powder composition, such as a depletion of heavier elements due to oxidation or inclusion in the melt slag, but in this case the reduction in true density would be homogeneous between the granulometric intervals analyzed. In fact, the original melt would have the same composition regardless of the final powder size. Interestingly, although in agreement with these results, Cui et al. [16] observed no significant effect of initial powder porosity on the porosity of super duplex steel printed by L-PBF.

3.2.3. Qualitative morphology

The atomized UNS S32760 powders exhibited high sphericity over the range of gas pressures applied, as shown in Fig. 8, with deviations from sphericity increasing for larger particles due to elongated shapes and satellite attachment. Higher gas pressures contributed to an increase in surface roughness and satellite formation, particularly evident in powders produced at 45 bar. This trend is consistent with the findings of Beckers et al. [15], who observed similar morphology changes in gas-atomized powders and attributed increased roughness and satellite formation to higher gas velocities and the resulting increase in particle impingement forces. The solidification microstructure in the UNS

S32760 powders was predominantly cellular/dendritic at all gas pressures, a common feature in the rapid cooling environments typical of gas atomization. This observation is consistent with previous reports by Yang et al. [31], who described similar cellular/dendritic structures in atomized stainless steel powders cooled at high gas velocities, indicating the influence of rapid cooling rates on solidification microstructures.

The cross-sectional SEM images in Fig. 9 show randomly distributed pores within the powders, with pore size generally increasing with particle size. The origin of these pores is currently debated, as their irregular shape supports the hypothesis that they may result from a solidification shrinkage mechanism. The formation of pores having different size as powder size changes is consistent with results reported by Bassini et al. [32] for Astroloy powders, where larger particles retained more internal porosity due to slower cooling rates, allowing trapped gas bubbles to coalesce. Urionabarrenetxea et al. [33] also found that high atomization gas pressures can lead to turbulent gas recirculation, which promotes satellite formation on powder surfaces. This effect is particularly evident for high-pressure atomized powders, where recirculating gas flows are likely contributing to satellite formation on larger particles. In addition, Wang et al. [25] provided insight into nozzle clogging and intermittent melt flow in high-pressure atomization, which can lead to inconsistent particle shapes and sizes. Such irregularities are evident in the powders atomized at 45 bar in this study, where occasional deviations from the expected sphericity and size distribution were observed. These variations may be due to nozzle instabilities and gas recirculation which disrupt steady melt flow and alter particle morphology during atomization. Overall, the morphology of UNS S32760 powders produced under different gas pressures highlights the trade-off between finer particle size and increased surface irregularities. Higher atomization pressures improved sphericity and reduced particle size, but also introduced greater satellite formation and internal porosity, reflecting both the benefits and challenges of optimizing gas atomization parameters for powder production.

In the case of large powders (i.e., 106–120 μm in Fig. 9), since the shape of the pores is not regular, their nature can be associated with the dual effect of gas entrapment and solidification shrinkage acting simultaneously. Irregular shrinkages compatible with rapid solidification and insufficient liquid are located near a more circular pore that would be characteristic for gas porosity. If the quasi-circular pore is due to gas entrapment, the heat transfer mechanisms would be locally altered, influencing the formation of shrinkage porosities. Specifically, a gas pore represents a region of thermal discontinuity within the solid or liquid structure. Gas is a poor heat conductor in comparison to metal, and the presence of a gas pore locally could reduce heat flow, delaying solidification in the adjacent areas.

3.2.4. Chemical composition

The composition of the powders is influenced by the gas atomization process, especially by the gas used in the melting and atomization stages [16]. In terms of light element concentration, melting in an argon shielding atmosphere and atomizing with argon as the inert gas is expected to reduce the amount of nitrogen according to Sievert's law, due to the low nitrogen partial pressure in the melting chamber. A reduction from 0.2 wt. % to 0.13 ± 0.02 wt. % was observed compared to the feedstock material (as shown in Fig. 10a). The melting phase accounts for the majority of nitrogen loss, as confirmed by the randomly scattered experimental data. Conversely, a systematic trend would have been observed if the atomizing gas pressure had a significant effect on the nitrogen content of the final powders. As with nitrogen, oxygen (Fig. 10b), carbon (Fig. 10c) and sulfur (Fig. 10d) were not expected to vary with atomization gas pressure because of their low volatility. An average amount of hydrogen ranging between 2 and 3 ppm was detected in the powders. This result has to be intended as an approximate value since hydrogen measurement by thermal evaporation method is not standardized. Particle size has been shown to have a strong influence on the oxygen uptake by the powders, as already documented in the
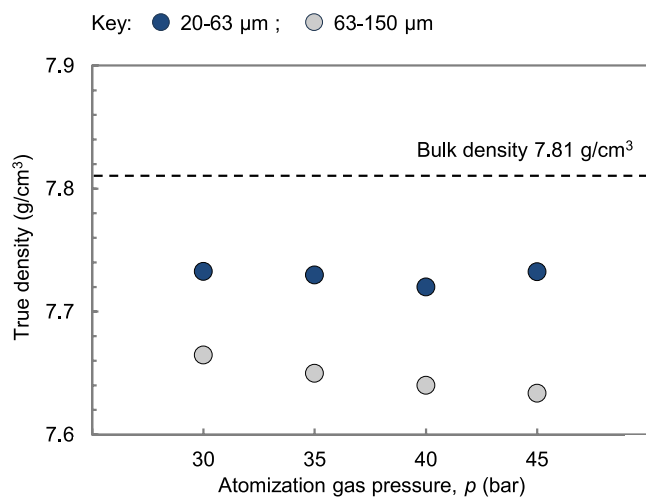

Fig. 7. True density for the atomized powders in the 20–63 μm and 63–150 μm ranges. Bulk density was calculated according to Ref. [30].
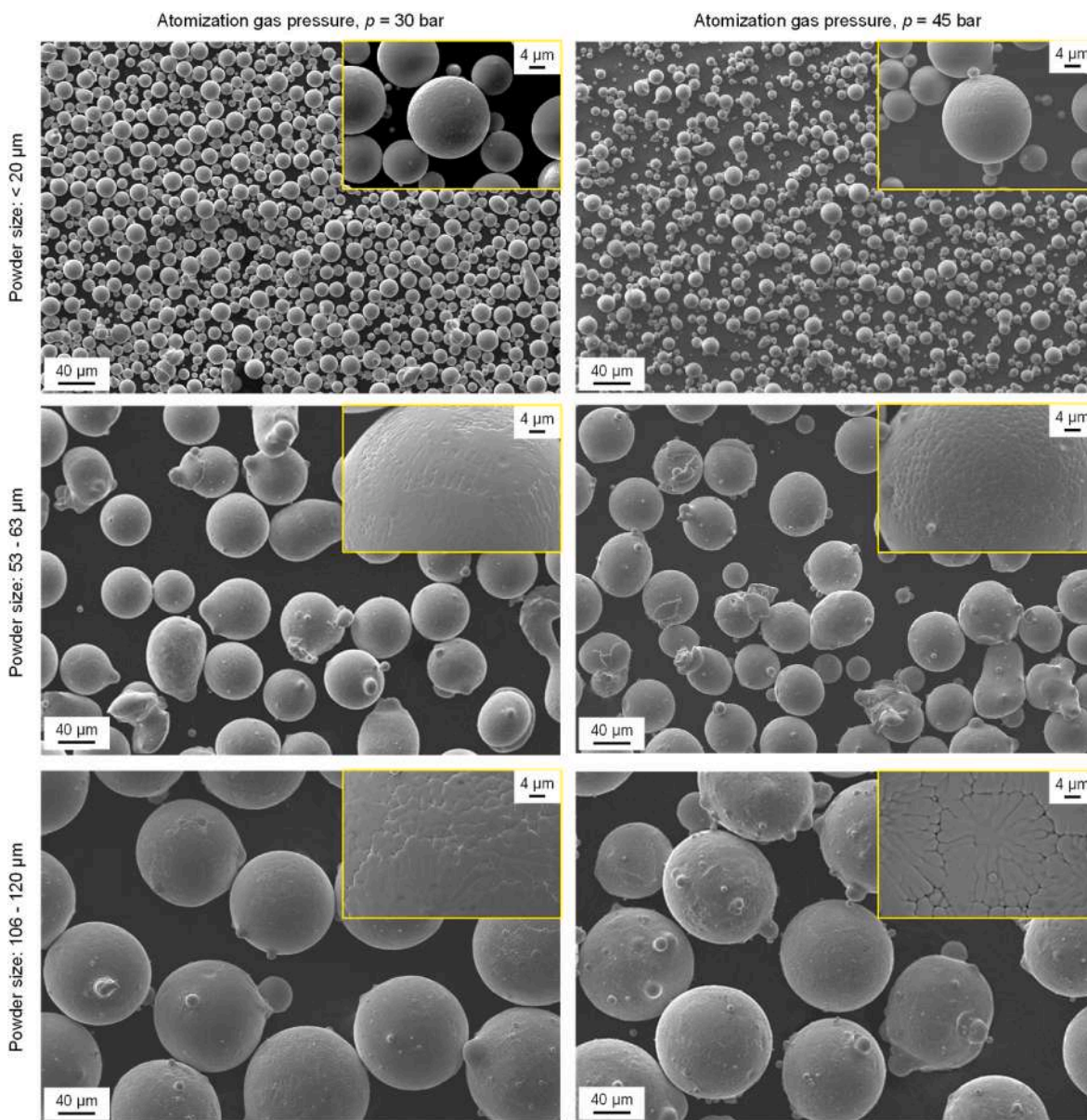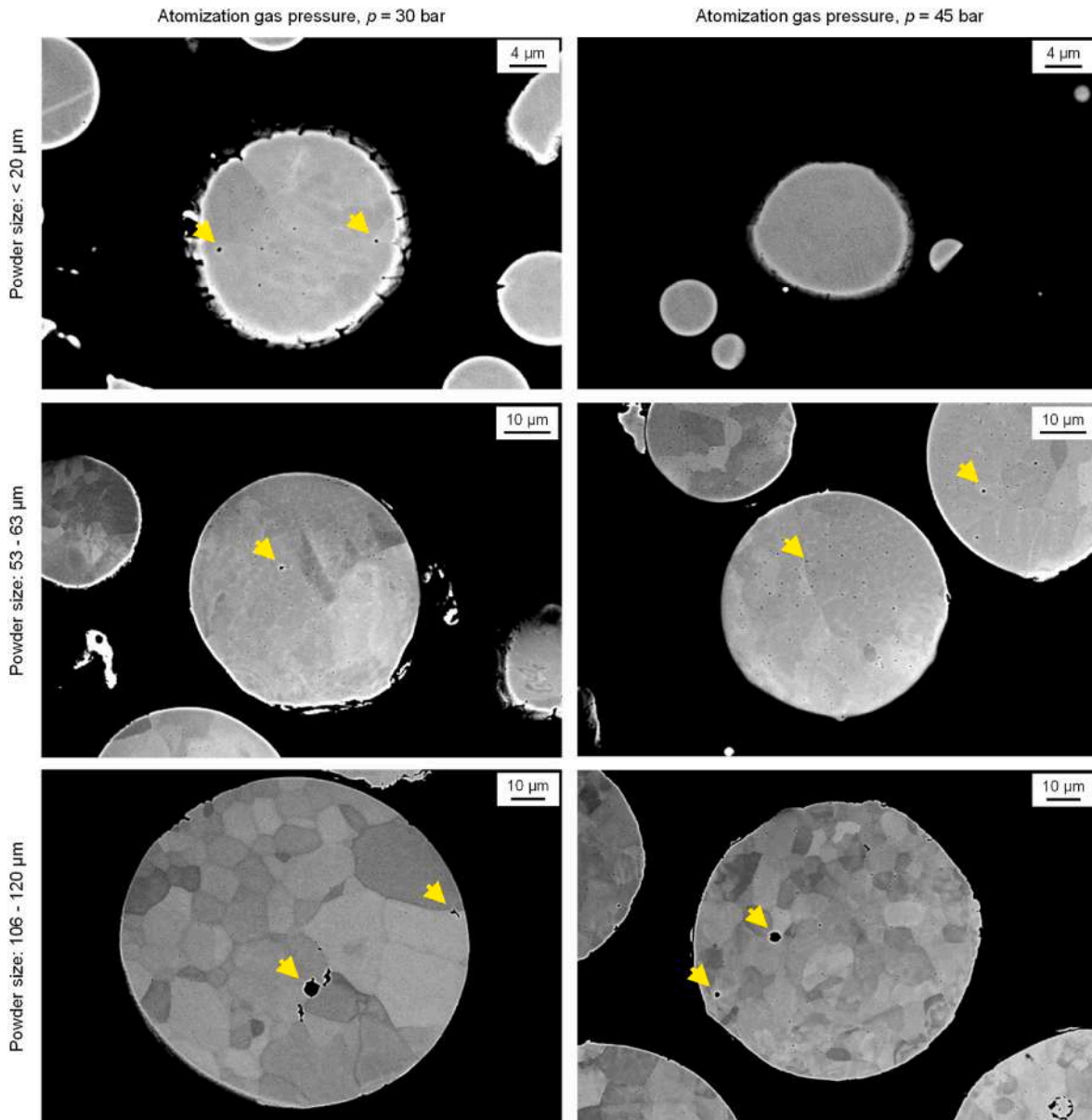
Fig. 8. SEM images of powders atomized at 30 bar (*left*) and 45 bar (*right*), after being sieved at narrow particle size ranges.

literature for nickel-based alloys [32]. The higher specific surface area characteristic of small powders contributes to an increase in the volume ratio between the amount of oxygen incorporated into the powders and that constituting the complex oxidized layer spontaneously formed on the surface of stainless steel powders.

Fig. 11 shows the effect of atomization gas pressure on chromium (Cr), molybdenum (Mo), and tungsten (W) for the two extreme range values of 30 and 45 bar. These elements are reported here because of their contribution to the determination of the Pitting Resistance Equivalent Number (PREN = %Cr + 3.3·(%Mo + 0.5·%W) + 16·%N), since their depletion can cause a reduction in PREN. No significant trend in the concentration of these elements is observed when the atomization gas pressure is varied, confirming that atomizing at higher or lower pressure does not affect the final powder composition when argon is used as the process gas. The depletion of nitrogen in the melt causes the PREN to decrease from 42.4 ± 5% for wrought material to 41.1 ± 5% for powders. However, the PREN number still exceeds the conventional lower limit (i.e., 40) that defines a super duplex stainless steel. As for the elements influencing the PREN index (Cr, Mo, and W), an ICP-OES analysis was also carried out on powder samples ranging from 2 to 4

g, giving results consistent with those of the EDS analysis, as shown in Table 5. Interestingly, no trace of titanium was detected despite its presence in the original composition. Titanium may have oxidized due to its high reactivity with oxygen; indeed, in its pure or alloyed form, it is typically melted either under high vacuum conditions with non-reactive refractories or using skull melting techniques [34].

The fast cooling rate of gas atomization resulted in the formation of a homogeneous microstructure in the powders, as shown by the EDS mapping in Fig. 12, and no segregation is observed for the main alloying elements both on the surface and in the cross-section of the powders analyzed. The statistical significance of the analysis performed on the single powder is also confirmed by an analysis on larger samples. Similar to welding [35] or L-PBF additive manufacturing processes [11], the intense cooling rate suppresses the δ → γ transformation in the solid state, resulting in a fully ferritic structure at room temperature (Fig. 13a), regardless of the atomization gas pressure and the resulting different cooling rate. It is also noteworthy that powders smaller than 20 μm and larger than 106 μm show a fully ferritic structure, even when comparing the two extreme pressure values used in the gas atomization tests. The raw material appears to have a balanced austenite/ferrite ratio

Fig. 9. SEM-BSE images of the cross-section of powders atomized at 30 bar (*left*) and 45 bar (*right*), after being sieved at narrow particle size ranges. Pores are indicated by arrows.

(Fig. 13*a*), according to the homogenization heat treatment it underwent prior to plastic deformation. Subtle variations appear when comparing the crystallite size of powders atomized at 30 or 45 bar (Fig. 13*b*). A significant difference in crystallite size is observed for larger powders as the gas pressure is increased. Powders atomized at a higher pressure show a smaller crystallite size, which is compatible with a higher cooling rate according to the literature [32].

3.2.5. Morphological properties

The morphology of powders and their flowability properties are closely related; more irregular powders have lower flowability, which affects both the density and the integrity of materials manufactured by L-PFB, DED [36], or hot isostatic pressing [32]. With regard to powder bed fusion technologies, the rheological properties of powders affect the formation of a uniform layer by the recoater and can be the source of defects [36]. The near-net-shape hot isostatic pressing technology is interested by the powder packing factor during capsule filling [32]. As for DED, it has been shown that a powder morphology closer to the ideal spherical shape could contribute to a finer microstructure and a more

obvious preferential orientation of the printed part [37]. The main morphological indicators of the atomized powders are presented in Fig. 14 as moving averages along the analyzed PSD.

All the powders tested show comparable and high values for all the indicators (namely: convexity, solidity, aspect ratio, and circularity), with the most regular morphological characteristics obtained for the powders atomized at 40 bar. As the powder size increases, the morphological indicators tend to decrease, an observation that can be explained by some process-related considerations. Increasing the atomization gas pressure, and consequently the gas velocity, makes the primary and secondary atomization mechanisms more efficient, leading to a shift in the PSD to lower values. However, two different side effects can occur when the gas pressure is increased: (*i*) freezing of the melt delivery nozzle [28] and (*ii*) turbulent recirculation in the atomization chamber. Both mechanisms lead to a deterioration of the powder morphology. More specifically, the PSD does not decrease when the gas pressure is increased from 40 to 45 bar because the atomization mechanisms are hindered by the intermittent flow and a likely limitation of the atomization unit [24]. On the other hand, the quality of the powders

Key: Atomization gas pressure, *p* = ● 30 bar ; ● 35 bar ; ● 40 bar ; ● 45 bar
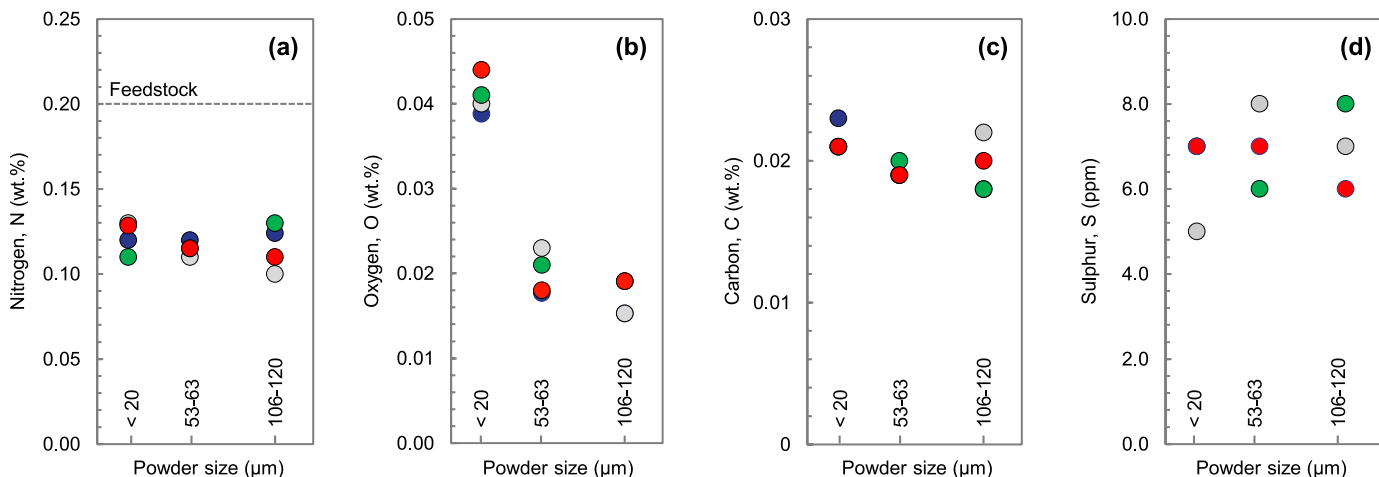

Fig. 10. Light element contents for isolated PSD intervals as measured by combustion and NDIR analysis according to ASTM E1019.

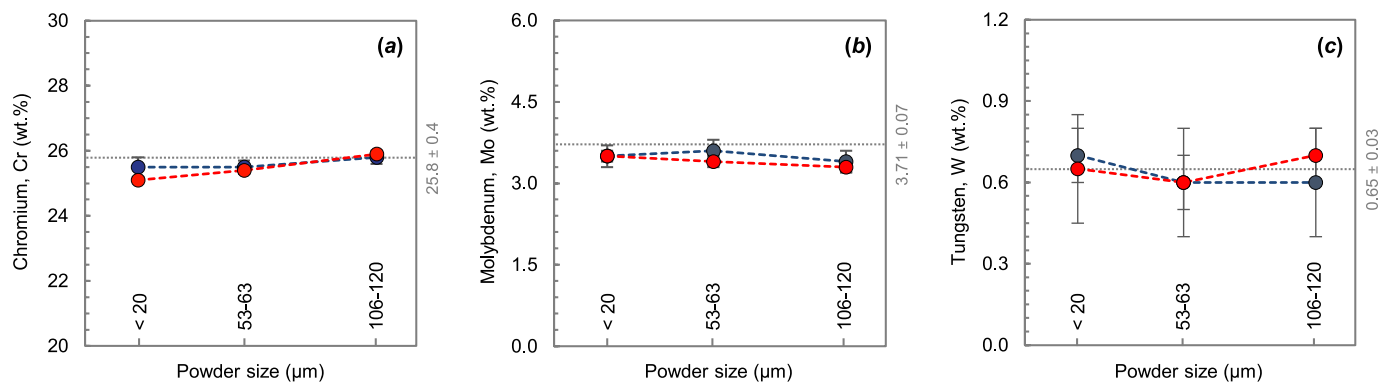Key: Atomization gas pressure, *p* = ● 30 bar ; ● 45 bar   (The dashed lines are a guide to the eye)

Fig. 11. Cr, Mo, and W contents for isolated PSD intervals as measured by EDS analysis on powder cross-sections.

Table 5
Average chemical composition as measured by ICP-OES for the powders atomized at 45 bar in the as-atomized condition.

Element	wt. %
Chromium, Cr	25.12 ± 0.004
Nickel, Ni	7.26 ± 0.002
Manganese, Mn	0.62 ± 0.005
Molybdenum, Mo	3.62 ± 0.003
Copper, Cu	0.61 ± 0.001
Tungsten, W	0.58 ± 0.004
Niobium, Nb	0.012 ± 0.004
Vanadium, V	0.031 ± 0.001
Cobalt, Co	0.065 ± 0.001
Silicon, Si	0.431 ± 0.001
Iron, Fe	61.65 ± 0.003

in terms of circularity is compromised by rapid cooling as the size of the powders increases. The spheroidization of larger particles (i.e., above 70 μm) is more affected by the cooling rate than that of small particles (i. e., below 30 μm). As the surface area to volume ratio decreases with increasing powder size, surface tension will play a minor role in the spheroidization of larger particles, and the spheroidization time will also decrease with decreasing gas temperature associated with higher gas expansion. The increasing gas flow in the atomization chamber due to the increase in gas pressure may be responsible for the formation of gas

recirculation in the upper part of the atomization tower, leading to the inclusion of satellites on the powder surfaces. Despite this observation, the other morphological properties related to the satellite content (in particular solidity and convexity) show a similar trend for the four different gas pressures, with a maximum variation within 2%. Finally, the powders atomized at 40 bar show slightly increased morphological properties, although all the other powders still show a high morphological quality.

3.3. Energy and carbon footprint results

An evaluation based solely on quality and metallurgical characterization may prove inadequate when different atomization conditions yield comparable outcomes. In such cases, environmental sustainability concerns warrant consideration. The carbon footprint and primary energy demand results were calculated in accordance with the aim and scope, system boundaries, and assumptions presented in Section 2.3, as a function of the data collection detailed in Section 3.3.1.

3.3.1. Data inventory
The analysis was based on both primary data, which were mainly gathered at the laboratory level, and secondary data, where the former were not available. When necessary, ranges were assumed to accommodate any potential uncertainty associated with the input values. The energy requirements were acquired by means of a Schneider PM 3250
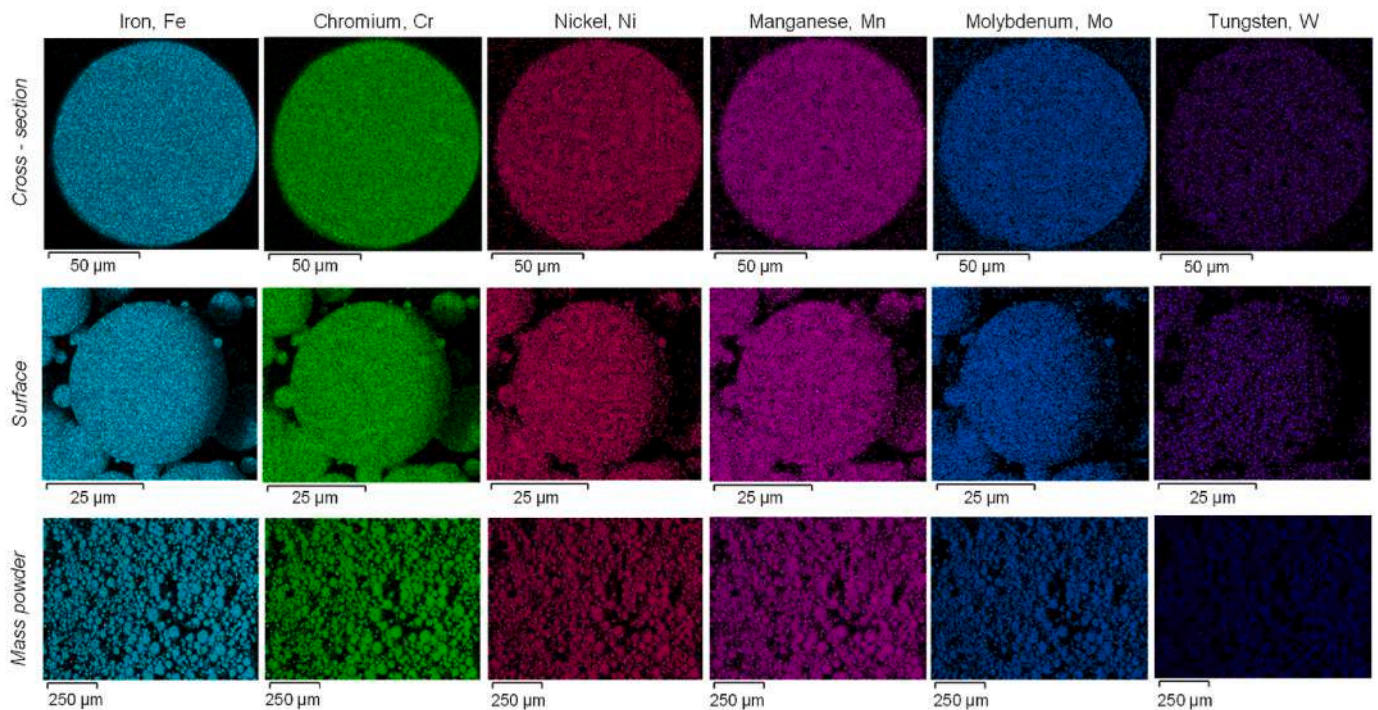
Fig. 12. Distribution of the ferrite/austenite stabilizing elements according to EDS mapping for powders atomized at 45 bar.
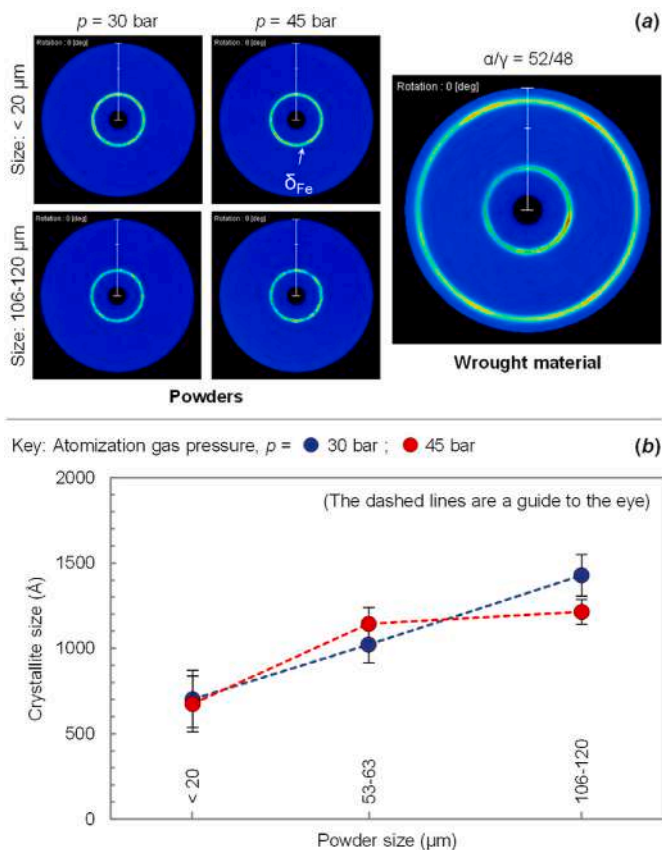

Fig. 13. Phase quantification by XRD according to the $\cos^2\alpha$ method (*a*) and crystallite size when gas atomizing at 30 and 45 bar (*b*).

electrical power analyzer, and the amount of gas used during atomization was measured by a Platon GMTX flowmeter installed on the high-pressure gas line. A previous dataset [17] was updated in accordance with the latest available data and expanded to calculate the primary energy demand. Details regarding the material and resource flows, as well as the impact factors, are provided in the following:

- *Powder material flows*. For each test, the crucible was loaded with 5.2 $\pm$ 0.3 kg of a mixture of non-compliant nuts and bolts. The atomization process resulted in an average material loss rate of 2%. This was attributed to the finer particles being trapped in the exhaust filters and chamber. The powder size distribution after sieving is shown in Table 6 as a function of atomization gas pressure (*p*). The debris exceeding 150 μm can be reused as feed material for a new atomization cycle. Considering only the fraction of useable powders having a size <150 μm, the average net process yield (i.e., the ratio of the mass of powders produced to the mass of feed material) increased with the atomization gas pressure, and varied between 80% for *p* = 30 bar and 88% for *p* = 45 bar. These values are comparable to data available in the literature, as in the review by Kokare et al. [38].

- *Electrical energy requirements*. The total energy consumption during gas atomization, inclusive of all equipment and auxiliary apparatus, was quantified at the laboratory scale and found to be 47.1 kWh per cycle [17]. This value remained constant for all tests, as the atomization cycle was not changed while the gas pressure (*p*) was varied. In addition, the energy requirements for cleaning (equal to 0.06 kWh per batch) and sieving were incorporated into the analysis. The 1.1 kW-rated sieve was monitored for a period of 4 h, during which 24 kg of powder was sieved. This resulted in a specific energy consumption of 0.183 kWh/kg. The GHG emission intensity of electricity generation was assumed to be 0.210 $kgCO_2$/kWh (EU-27 average for 2023), according to the latest data from the European Environment Agency [39]. A primary-to-secondary energy conversion factor of 0.38 was considered.

- *Argon consumption*. The total argon consumption is given in Table 3 for reference. The carbon footprint was assumed to be 0.18 $\pm$ 10% $kgCO_2$/kg argon, as calculated from cradle-to-gate (including

Key: Atomization gas pressure, *p* = ● 30 bar ; ● 35 bar ; ● 40 bar ; ● 45 bar
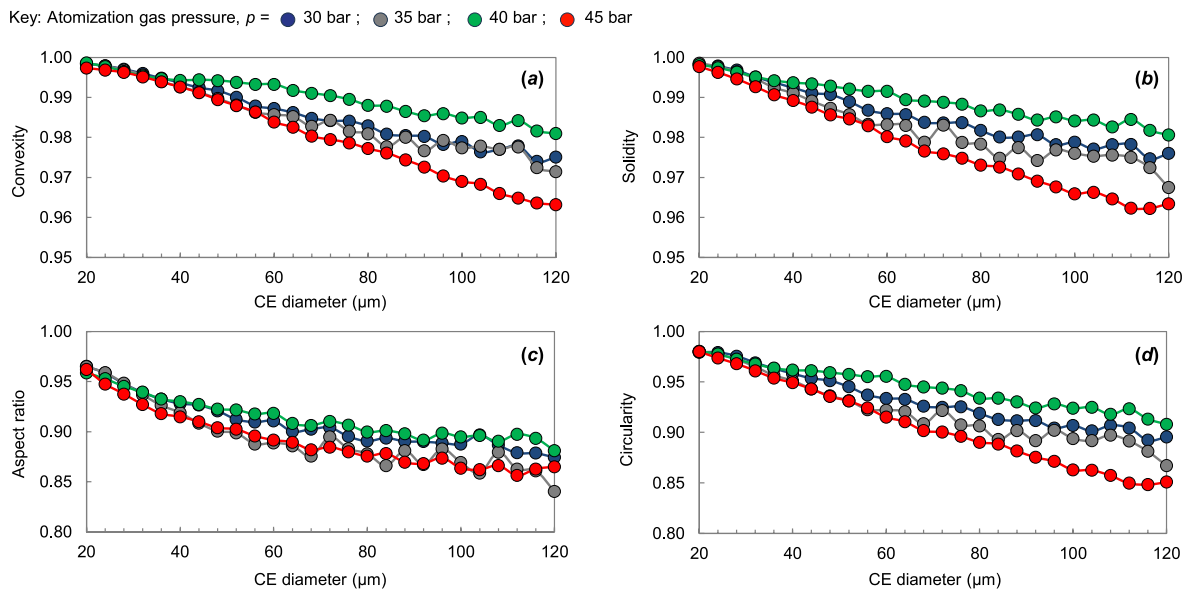

Fig. 14. Quantitative morphological properties of powders measured by automated optical imaging analysis: convexity (*a*), solidity (*b*), aspect ratio (*c*), and circularity (*d*).

Table 6
Powder size distribution after sieving [17].

Powder size	Atomization gas pressure, *p*			
	30 bar	35 bar	40 bar	45 bar
<20 μm	4.2 vol. %	6.4 vol. %	8.1 vol. %	8.3 vol. %
20–63 μm	28.8 vol. %	38.6 vol. %	39.9 vol. %	43.7 vol. %
63–150 μm	49.0 vol. %	41.0 vol. %	42.0 vol. %	38.2 vol. %
>150 μm	18.0 vol. %	14.0 vol. %	10.0 vol. %	9.8 vol. %

delivery to the atomization site) primary data made available by the supplier [17]. This value is higher than that reported in other literature sources, which typically do not consider the effects of gas storage and transportation. For example, Lavery et al. [40] assumed an energy input requirement of 0.102 kWh/kg for argon production in their life cycle assessment (LCA) of gas atomized sponge nickel catalysts, while Kamps et al. [41] considered 0.692 MJ/kg argon in their LCA of steel gear production by laser beam melting. Based on the current European greenhouse gas emission intensity of electricity generation, this would have resulted in a carbon footprint of less than 0.05 kgCO$_2$/kg argon. Therefore, in the absence of publicly available data, the embodied primary energy was proportionally and conservatively assumed to be 8.1 ± 20% MJ/kg argon.

- *Refractories.* The consumable components made of refractory materials are listed in Table 7, which also includes information on the number of uses before replacement (since the material to be processed is the same, there are no problems related to contamination phenomena). For the purpose of the calculation, all the environmental impacts were related to the primary production of the

Table 7
Consumable refractory materials for the gas atomization process.

Component	Mass	Main material	Number of uses before replacement
Crucible	3.4 kg	Alumina	3
Stopper rod	0.1 kg	Alumina	3
Crucible insert	28.5 g	Alumina	3
Melt delivery tube	2.2 g	Alumina	1
Melt delivery nozzle	0.8 g	Boron nitride (proxy)	1

refractories. In addition, although the abraded crucible can be repaired with an alumina cement coating, it is supposed that all consumables are disposed of at the end of their useful life. The carbon footprint and embodied energy for the primary production of high-purity (99.5%) alumina were assumed to be 2.81 ± 5% kgCO$_2$/kg and 52.1 ± 5% MJ/kg, respectively [42]. The melt delivery nozzle is made of a mixture of refractory materials: BN, ZrO$_2$, and SiC. The main component is boron nitride, which is used as a proxy material for the assessment (with a carbon footprint and embodied energy of 6.82 ± 5% kgCO$_2$/kg and 126.5 ± 5% MJ/kg, respectively [42]).

- *Solvents.* The atomization process required 0.2 kg of acetone per cycle [17], and 0.5 kg of an acetone-based mixed solvent was used for the preliminary ultrasonic cleaning of the non-compliant parts. The carbon footprint and the primary energy demand for acetone or acetone-based solvents were assumed to be 2.0 ± 30% kgCO$_2$/kg and 65 ± 30% MJ/kg, respectively, taking into account the values available in technical reports and eco-profiles [43,44]. In addition, the specific consumption of ethanol for cleaning the sieve when the material to be sieved is changed appears to be negligible on a unit-mass basis assessment.

3.3.2. Powder size-dependent carbon footprint

The results obtained for the primary energy demand (E_{Batch}) and equivalent CO$_2$ emissions ($CO_{2\ Batch}$) for the processing (cleaning, atomizing, and sieving) of a 5.2 ± 0.3 kg batch of material are presented in Fig. 15*a* and *b*, respectively. Fig. 15*c* shows the resulting CO$_2$ emissions per unit mass of powder of a given size, which are related to the results presented in Fig. 15*b* according to Equation (1),

$$CO_{2\ Batch} = CE_{< 20\ \mu m} \cdot m_{< 20\ \mu m} + CE_{20-63\ \mu m} \cdot m_{20-63\ \mu m}$$
$$+ CE_{63-150\ \mu m} \cdot m_{63-150\ \mu m} \tag{1}$$

where:

- $CO_{2\ Batch}$ (kgCO$_2$) is the total amount of CO$_2$ emissions per atomized and sieved batch, as shown in Fig. 15*b*;
- CE_i (kgCO$_2$/kg) is the amount of CO$_2$ emissions per unit mass of powder having a granulometry $i < 20$ μm, or equal to 20–63 μm, or equal to 63–150 μm, as shown in Fig. 15*c*;
- m_i (kg) is the mass of the powder of granulometry i obtained from the atomization and sieving of each batch.
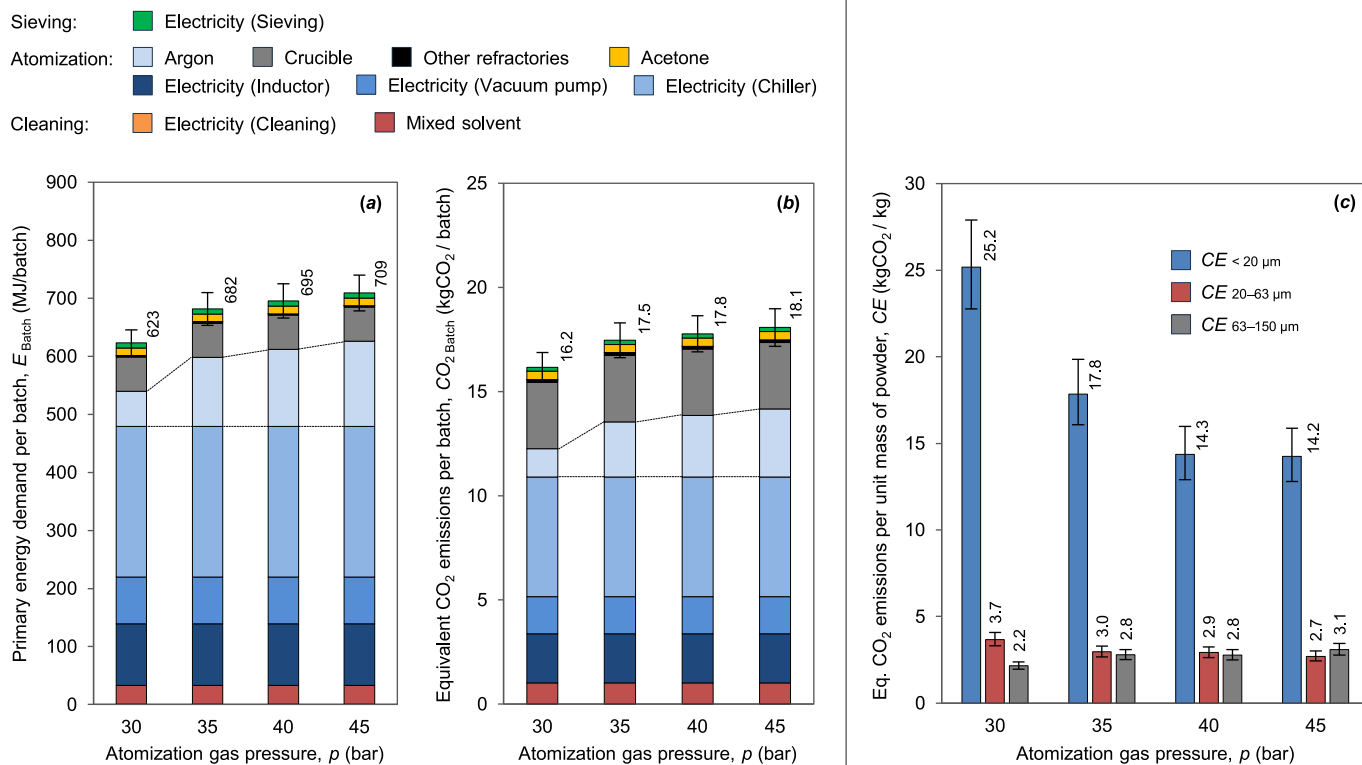
Fig. 15. Primary energy demand (*a*) and equivalent CO_2 emissions (*b*) per batch, and carbon footprint as a function of powder size (*c*).

Equation (1) allocates the total CO_2 emissions (or the total primary energy demand, if energy parameters are considered) per batch in proportion to the different amounts of useful powders having sizes of <20 μm, 20–63 μm, and 63–150 μm, which have been obtained when varying test conditions (Table 6). This analysis considers the practical applications of the powders, which can be used as feedstock for diverse processes (from L-PBF to MIM), and enables the comparative assessment of different atomization gas pressures.

While the findings of this study are limited to the specific case and the laboratory scale under consideration, and should therefore be extended to other contexts with due caution, a similarity can be observed between the results of primary energy demand and CO_2 emissions. The main driver of both is the electricity consumption during the atomization phase. Moreover, based on the assumptions presented in Section 3.3.1, the variation in the results is solely attributable to the increase in argon consumption as the atomization gas pressure increases (Table 3). The contribution of refractories (other than the alumina crucible), solvents, cleaning, and sieving appears to be either negligible or of secondary importance (Fig. 15*a* and *b*). As the atomization gas pressure (*p*) is increased, the CO_2 emissions per unit mass of powder produced (Fig. 15*c*) decrease significantly for powders smaller than 20 μm and, to a lesser extent, for powders sized between 20 and 63 μm. Powders in the 63–150 μm range, however, exhibit the opposite behavior, although again the variations remain limited. This evidence is consistent with the powder size distribution results (see Table 6), as the increase in atomization gas pressure results in higher fractions of smaller powders and an increase in the average net process yield [17].

A direct comparison of the results presented in Fig. 15 with the available literature sources on metal powder production (see Ref. [38] and references therein) is hindered by several factors. Few studies focus on the environmental impact of super duplex steel powders. Most research on other materials considers only the electricity and argon consumption during atomization, without including the pre- and post-atomization processes and/or the impact of consumables. Additionally, the available data is often aggregated, making it difficult to

separate the environmental impact of the atomization process itself from that of the processed material. To allow comparability between different energy levels, the electrical energy values in Fig. 15*a* have been corrected back to a fossil fuel equivalent according to the relationship 1 kWh = 3.6 MJ electrical energy = 3.6/0.38 oil equivalent MJ, where 0.38 is the assumed primary-to-secondary conversion efficiency [45]. If the analysis is limited to the electricity requirements of gas atomization alone, the values obtained in this study range from 7.0 to 10.7 kWh/kg for powders of 20–63 μm, and from 6.3 to 8.1 kWh/kg for powders of 63–150 μm. These values appear to be generally higher than those reported in LCA analyses of additive manufacturing processes [38] using stainless steel powders (e.g., 2 kWh/kg powder [46]), and comparable or lower when using other materials, such as Ti–6Al–4V (e.g., 6.6 kWh/kg powder [47]) or Inconel (15.4 kWh/kg and 6.85 kgCO₂/kg powder, handling the data in Ref. [48]). Nonetheless, a meaningful comparison of the available results should consider not only the differences in materials, but also the variations in atomization processes, equipment used, and the impact factors assumed in the analysis.

3.3.3. Benefits of direct waste recycling

Producing powders directly from industrial waste offers a technological alternative to traditional material recycling methods, further enhancing closed-loop material flows central to sustainable manufacturing and supporting the implementation of the 'industrial symbiosis' [49,50]. This can result in significant benefits in terms of reduced CO_2 emissions compared to conventional powder production from primary and/or secondary feedstocks (i.e., the Scenario 'B' in Fig. 3), as already highlighted by the research of Benedetti et al. [20]. The average carbon footprint for the production of a UNS S32760 duplex stainless steel in the solution annealed condition is 5.4 ± 5% kgCO₂/kg for primary production and 1.3 ± 7% kgCO₂/kg for secondary production [42]. Assuming a recycled content in the current material supply of 0.37 ± 5% [42] and following the recycled content approach proposed by Hammond and Jones [51], this would result in an effective carbon footprint of 3.9 ± 7% kgCO₂ per kg of raw material. According to the

Scenario 'B' in Fig. 3, this value should be added to the results shown in Fig. 15c, assuming the same gas atomization process is used. Even without considering possible contributions from pre-manufacturing and material preparation, this factor alone would more than double the carbon footprint for powders with coarser particle sizes (20–63 μm or 63–150 μm) and increase it by 15%–28% for those <20 μm, which are already characterized by a significant process environmental impact.

4. Conclusions

The effect of atomization gas pressure on the quality and carbon footprint of inert-gas atomized UNS S32760 powders was investigated in this study. Gas pressure appears to be a critical factor in determining the process efficiency and final properties of super duplex stainless steel powders for additive manufacturing applications, as its increase reduces the average particle size. However, it is necessary to evaluate the trade-offs in producing powders tailored to a specific additive manufacturing process. The main findings of this research can be summarized as follows:

- higher gas pressure improves atomization efficiency, but also increases gas consumption and results in longer atomization times;
- gas cooling during expansion can cause instability in the atomization plume, resulting in intermittent melt interruptions and powder size distribution (PSD) variations. This phenomenon becomes more pronounced at higher gas pressures as the cooling effect increases with gas expansion. The resulting instability can affect the consistency and quality of the powders produced;
- morphological analysis has shown that higher gas pressure can increase surface irregularities and pore formation, especially as powder size increases. While tighter atomization plumes at higher pressures improve powder sphericity and flowability, the rapid cooling associated with higher pressures can lead to increased surface roughness and pore formation within powders;
- chemical composition analysis revealed that gas pressure has minimal effect on powder composition when argon is used as the inert gas. The composition of the powders remains relatively unaffected by changes in gas pressure, indicating that variations in atomization pressure primarily affect physical properties rather than chemical composition;
- the primary energy demand and the carbon footprint analyses showed that higher gas pressure increases the environmental impact per produced batch, mainly due to the increased gas consumption. However, the results show a significant decrease in CO_2 emissions per unit mass with increasing atomization gas pressure, especially for smaller powders.

Overall, the recycling of manufacturing waste allows the immediate reintroduction of secondary materials into the life cycle of other products, reducing the consumption of resources to meet the growing demand for engineered materials. Optimizing atomization gas pressure is critical to achieving desired powder properties while minimizing environmental impact. An atomization pressure of 40 bar was found to be suitable to balance efficiency, powder properties and CO_2 emissions for the production of UNS S32760 powders with the equipment and setup used in this research. Although this is a case study for a specific material, the approach proposed here can serve as a basis for the development of a quantitative method for assessing powder quality and sustainability in different alloys, based on the cross-evaluation of quality and sustainability indicators. These findings could provide valuable insights for improving powder production processes in additive manufacturing, thereby contributing to the advancement of sustainable manufacturing practices.

Declaration of competing interest

The authors declare that they have no known competing financial interests or personal relationships that could have appeared to influence the work reported in this paper.

References

[1] Francis R, Byrne G. Duplex stainless steels—alloys for the 21st century. Metals 2021;11(5):836. https://doi.org/10.3390/met11050836.

[2] Hänninen H, Romu J, Ilola R, Tervo J, Laitinen A. Effects of processing and manufacturing of high nitrogen-containing stainless steels on their mechanical, corrosion and wear properties. J Mater Process Technol 2001;117:424–30. https://doi.org/10.1016/S0924-0136(01)00804-4.

[3] Panagopoulos A, Loizidou M, Haralambous KJ. Stainless steel in thermal desalination and brine treatment: current status and prospects. Met Mater Int 2020; 26:1463–82. https://doi.org/10.1007/s12540-019-00398-w.

[4] Gatto ML, Santoni A, Santecchia E, Spigarelli S, Fiori F, Mengucci P, Cabibbo M. The potential of duplex stainless steel processed by laser powder bed fusion for biomedical applications: a review. Metals 2023;13(5):949. https://doi.org/10.3390/met13050949.

[5] Tseng CM, Liou HY, Tsai WT. The influence of nitrogen content on corrosion fatigue crack growth behavior of duplex stainless steel. Mater Sci Eng, A 2003;344: 190–200. https://doi.org/10.1016/S0921-5093(02)00404-5.

[6] Alvarez-Armas I, Degallaix-Moreuil S, editors. Duplex stainless steels; 2013. https://doi.org/10.1002/9781118557990.

[7] Dobrzański LA, Brytan Z, Grande MA, Rosso M, Pallavicini EJ. Properties of vacuum sintered duplex stainless steels. J Mater Process Technol 2005;162–163: 286–92. https://doi.org/10.1016/j.jmatprotec.2005.02.038.

[8] Smuk O, Nenonen P, Hänninen H, Liimatainen J. Microstructures of a powder metallurgy-hot-isostatically pressed super duplex stainless steel forming in industrial heat treatments. Metall Mater Trans A Phys Metall Mater Sci 2004;35(A): 2103–9. https://doi.org/10.1007/s11661-004-0158-9.

[9] Zhang D, Liu A, Yin B, Wen P. Additive manufacturing of duplex stainless steels - a critical review. J Manuf Process 2022;73:496–517. https://doi.org/10.1016/j.jmapro.2021.11.036.

[10] Gargalis L, Karavias L, Graff JS, Diplas S, Koumoulos EP, Karaxi EK. A comparative investigation of duplex and super duplex stainless steels processed through laser powder bed fusion. Metals 2023;13(11):1897. https://doi.org/10.3390/met13111897.

[11] Iams AD, Keist JS, Palmer TA. Formation of austenite in additively manufactured and post-processed duplex stainless steel alloys. Metall Mater Trans A Phys Metall Mater Sci 2020;51:982–99. https://doi.org/10.1007/s11661-019-05562-w.

[12] Zhang Y, Wu S, Cheng F. A specially-designed super duplex stainless steel with balanced ferrite:austenite ratio fabricated via flux-cored wire arc additive manufacturing: microstructure evolution, mechanical properties and corrosion resistance. Mater Sci Eng, A 2022;854:143809. https://doi.org/10.1016/j.msea.2022.143809.

[13] Roos S, Barbera Flichi F, Ortiz-Membrado L, Botero Vega CA, Jiménez-Piqué E, Rännar LE. Assessing the viability of high-frequency spot melting for super duplex stainless steel 2507 via electron beam powder bed fusion. J Mater Res Technol 2023;27:5720–8. https://doi.org/10.1016/j.jmrt.2023.11.028.

[14] Spierings AB, Voegtlin M, Bauer T, Wegener K. Powder flowability characterisation methodology for powder-bed-based metal additive manufacturing. Prog Addit Manuf 2016;1:9–20. https://doi.org/10.1007/s40964-015-0001-4.

[15] Beckers D, Ellendt N, Fritsching U, Uhlenwinkel V. Impact of process flow conditions on particle morphology in metal powder production via gas atomization. Adv Powder Technol 2020;31(1):300–11. https://doi.org/10.1016/j.apt.2019.10.022.

[16] Cui C, Stern F, Ellendt N, Uhlenwinkel V, Steinbacher M, Tenkamp J, Walther F, Fechte-Heinen R. Gas atomization of duplex stainless steel powder for laser powder bed fusion. Materials 2023;16(1):435. https://doi.org/10.3390/ma16010435.

[17] Gobber FS, Pennacchio A, Actis Grande M, Priarone P. An approach to evaluate quality and sustainability for powders produced by A Lab – scale atomizer. Euro PM 2024. Proc., EPMA; 2024. https://doi.org/10.59499/EP246282648.

[18] Pennacchio A, Gobber FS, Actis Grande M. Effect of process gas composition on the characteristics of atomised UNS S32760 duplex stainless steels powders. Euro PM 2023 Proc., EPMA 2023. https://doi.org/10.59499/EP235765086.

[19] Gobber FS, Actis Grande M. Effect of processing parameters on the characteristics of UNS 32760 duplex stainless steels powders. World PM 2022 Proc., EPMA 2022. https://doi.org/10.59499/WP225372042.

[20] Benedetti M, Perini M, Vanazzi M, Giorgini A, Macoretta G, Menapace C. Atomized scrap powder feedstock for sustainable Inconel 718 additive manufacturing via LPBF: a study of static and fatigue properties. Prog Addit Manuf 2024;9:1843–56. https://doi.org/10.1007/s40964-023-00547-z.

[21] Urionabarrenetxea E, Martín JM, Avello A, Rivas A. Simulation and validation of the gas flow in close-coupled gas atomisation process: influence of the inlet gas pressure and the throat width of the supersonic gas nozzle. Powder Technol 2022; 407:117688. https://doi.org/10.1016/j.powtec.2022.117688.

[22] Ünal R. The influence of the pressure formation at the tip of the melt delivery tube on tin powder size and gas/melt ratio in gas atomization method. J Mater Process Technol 2006;180(1–3):291–5. https://doi.org/10.1016/j.jmatprotec.2006.06.018.

[23] Liu H, Lavernia EJ, Rangel RH. An analysis of freeze-up phenomena during gas atomization of metals. Int J Heat Mass Tran 1995;38(12):2183–93. https://doi.org/10.1016/0017-9310(94)00345-V.

[24] Ünal R. Investigation on metal powder production efficiency of new convergent divergent nozzle in close coupled gas atomisation. Powder Metall 2007;50(4): 302–6. https://doi.org/10.1179/174329007X189595.

[25] Wang J, Xia M, Wu J, Jian X, Ge C. Precise control of atomization initial stage to address nozzle clogging issue in the vacuum induction-melting gas atomization process. J Mater Res Technol 2024;30:1505–17. https://doi.org/10.1016/j.jmrt.2024.03.095.

[26] Urionabarrenetxea E, Martín JM, Avello A. Influence of some geometric features of the atomisation chamber on particle agglomeration and satellite formation during gas atomisation. Euro PM 2019 congr exhib. 2019.

[27] Wood JV. Atomisation of melts for powder production and spray deposition. Int Mater Rev 1995;40(2):96. https://doi.org/10.1179/imr.1995.40.2.96.

[28] Urionabarrenetxea E, Avello A, Rivas A, Martín JM. Experimental study of the influence of operational and geometric variables on the powders produced by close-coupled gas atomisation. Mater Des 2021;199:109441. https://doi.org/10.1016/j.matdes.2020.109441.

[29] Li X, Zhu Q, Shu S, Fan J, Zhang S. Fine spherical powder production during gas atomization of pressurized melts through melt nozzles with a small inner diameter. Powder Technol 2019;356:759–68. https://doi.org/10.1016/j.powtec.2019.09.023.

[30] Mills KC, Su Y, Li Z, Brooks RF. Equations for the calculation of the thermo-physical properties of stainless steel. ISIJ Int 2004;44(10):1661–8. https://doi.org/10.2355/isijinternational.44.1661.

[31] Yang X, Gao F, Tang F, Hao X, Li Z. Effect of surface oxides on the melting and solidification of 316L stainless steel powder for additive manufacturing. Metall Mater Trans A Phys Metall Mater Sci 2021;52:4518–32. https://doi.org/10.1007/s11661-021-06405-3.

[32] Bassini E, Galech U, Soria T, Aristizabal M, Iturriza I, Biamino S, Ugues D. Effect of the particle size distribution on physical properties, composition, and quality of gas atomized Astroloy powders for HIP application. J Alloys Compd 2022;890:161631. https://doi.org/10.1016/j.jallcom.2021.161631.

[33] Urionabarrenetxea E, Martín JM, Rivas A, Castro F. Influence of the atomiser geometry on the gas flow in close-coupled gas atomisation. Proc Euro PM 2017 Int Powder Metall Congr Exhib 2017.

[34] Fashu S, Lototskyy M, Davids MW, Pickering L, Linkov V, Tai S, et al. A review on crucibles for induction melting of titanium alloys. Mater Des 2020;186:108295. https://doi.org/10.1016/j.matdes.2019.108295.

[35] Wang T, Phelan D, Wexler D, Qiu Z, Cui S, Franklin M, et al. New insights of the nucleation and subsequent phase transformation in duplex stainless steel. Mater Char 2023;203:113115. https://doi.org/10.1016/j.matchar.2023.113115.

[36] Capozzi LC, Sivo A, Bassini E. Powder spreading and spreadability in the additive manufacturing of metallic materials: a critical review. J Mater Process Technol 2022;308:117706. https://doi.org/10.1016/j.jmatprotec.2022.117706.

[37] Wang Z, Wang J, Xu S, Liu B, Sui Q, Zhao F, et al. Influence of powder characteristics on microstructure and mechanical properties of Inconel 718 superalloy manufactured by direct energy deposition. Appl Surf Sci 2022;583: 152545. https://doi.org/10.1016/j.apsusc.2022.152545.

[38] Kokare S, Oliveira JP, Godina R. Life cycle assessment of additive manufacturing processes: a review. J Manuf Syst 2023;68:536–59. https://doi.org/10.1016/j.jmsy.2023.05.007.

[39] European Environment Agengy (EEA). Greenhouse gas emission intensity of electricity generation, country level. https://www.eea.europa.eu/en/analysis/indicators/greenhouse-gas-emission-intensity-of-1/greenhouse-gas-emission-intensity-of-electricity-generation-country-level. [Accessed 10 November 2024].

[40] Lavery NP, Jarvis DJ, Brown SGR, Adkins NJ, Wilson BP. Life cycle assessment of sponge nickel produced by gas atomisation for use in industrial hydrogenation catalysis applications. Int J Life Cycle Assess 2013;18:362–76. https://doi.org/10.1007/s11367-012-0478-8.

[41] Kamps T, Lutter-Guenther M, Seidel C, Gutowski T, Reinhart G. Cost- and energy-efficient manufacture of gears by laser beam melting. CIRP J Manuf Sci Technol 2018;21:47–60. https://doi.org/10.1016/j.cirpj.2018.01.002.

[42] Ces Selector. Update 1, 17.2.0. the UK: Granta Design Limited; 2017.

[43] Azapagic A, Amienyo D, Cuéllar Franca RM, Jeswani HK. Carbon footprints of recycled solvents - study for the European solvent recycler group (ESRG) - august 2013. www.ethosresearch.co.uk. [Accessed 10 November 2024].

[44] European Solvents Industry Group (ESIG). Eco-profile of three oxygenated solvent (groups): n-butanol, butyl glycol ethers, acetone - november 2021. www.esig.org. [Accessed 10 November 2024].

[45] Ashby MF. Materials and the environment - eco-informed material choice. third ed. Butterworth-Heinemann; 2021. ISBN: 978-0-12-821521-0.

[46] Peng T, Wang Y, Zhu Y, et al. Life cycle assessment of selective-laser-melting produced hydraulic valve body with integrated design and manufacturing optimization: a cradle-to-gate study. Addit Manuf 2020;36:101530. https://doi.org/10.1016/j.addma.2020.101530.

[47] Paris H, Mokhtarian H, Coatanéa E, Museau M, Flores Ituarte I. Comparative environmental impacts of additive and subtractive manufacturing technologies. CIRP Ann - Manuf Technol 2016;65(1):29–32. https://doi.org/10.1016/j.cirp.2016.04.036.

[48] Torres-Carrillo S, Siller HR, Vila C, López C, Rodríguez CA. Environmental analysis of selective laser melting in the manufacturing of aeronautical turbine blades. J Clean Prod 2020;246:119068. https://doi.org/10.1016/j.jclepro.2019.119068.

[49] Jawahir IS, Bradley R. Technological elements of circular economy and the principles of 6R-based closed-loop material flow in sustainable manufacturing. Procedia CIRP 2016;40:103–8. https://doi.org/10.1016/j.procir.2016.01.067.

[50] Duflou JR, Wegener K, Tekkaya AE, Hauschild M, Bleicher F, Yan J, Hendrickx B. Efficiently preserving material resources in manufacturing: industrial symbiosis revisited. CIRP Ann - Manuf Technol 2024;73(2):695–721. https://doi.org/10.1016/j.cirp.2024.05.006.

[51] Hammond G, Jones C. Embodied carbon - the inventory of carbon and energy (ICE), annex B: how to account for recycling. ©BSRIA BG 10/2011 2011;8:117–28. ISBN 978 0 86022 703 8.